FDR4LDYN
Fundamental Data Record for Land Dynamic

ESA RFP/3-18440/24/I-DT-I

Algorithm Theoretical Basis Document (ATBD)

DT2-1

Revision History

Revision	Date	Author(s)	Description
0.1	20 June 2025	TU Wien	Preliminary version
1.0	1 October 2025	TU Wien	FDR4LDYN data record v0.1 release
1.5	8 July 2026	TU Wien	FDR4LDYN Case Study Review 1 update

How to cite this document

ESA, TU Wien, TU Delft, *Algorithm Theoretical Basis Document (ATBD) ERS ESCAT Fundamental Data Record for Land Dynamics 12.5 km sampling*, v1.5, 2026

Table of Contents

1 Executive summary

The Algorithm Theoretical Basis Document (ATBD) provides a comprehensive description of the retrieval methods and processing chain used to generate the FDR4LDYN data products. These products are derived from C-band backscatter observations collected by the scatterometers (ESCAT) onboard the European Remote Sensing satellites ERS-1 and ERS-2. The core variables provided in the main FDR4LDYN data record are normalized backscatter, slope, and curvature, together with relevant flags indicating their quality. This record is complemented by separate FDR4LDYN products containing ancillary parameters such as yearly azimuthal correction terms, uncertainty estimates, and advisory flags. Moreover, different variants of the slope and curvature time series will be included in future FDR4LDYN data products to address different application requirements. The data records are designed to ensure optimal interoperability with the corresponding current Metop ASCAT and future Metop-SG SCA backscatter observables, supporting the creation of a consistent long-term record of land surface backscatter. The FDR4LDYN products enable the monitoring of land surface dynamics and support diverse scientific and operational applications in domains such as soil moisture estimation, vegetation dynamics, flood monitoring, cryospheric research, and climate studies.

2 Introduction

2.1 Purpose of the document

The Algorithm Theoretical Basis Document (ATBD) is intended to provide a detailed description of the scientific background and theoretical justification behind the algorithm utilized for the FDR4LDYN data products based on C-band backscatter observations collected by the scatterometers (ESCAT) onboard the European Remote Sensing satellites ERS-1 and ERS-2.

2.2 Targeted audience

This document mainly targets:

1. Remote sensing experts interested in the retrieval and error characterization of satellite backscatter observable data sets.
2. Users of backscatter, slope, and curvature data sets who want to obtain a more in-depth understanding of the algorithm and sources of error.

3 ESCAT onboard ERS-1 and ERS-2

3.1 ERS missions

The first European Remote Sensing satellite, ERS-1, was launched by ESA on 17 July 1991 from Kourou, French Guiana [1]. As a major precursor to Europe's current Earth observation missions, ERS-1 built upon development efforts and feasibility studies initiated in the early 1970s [2]. ERS-1 carried a suite of instruments designed for comprehensive environmental monitoring of land, water, ice, and atmosphere. The mission's primary instrument was the Active Microwave Instrument (AMI), which combined a synthetic aperture radar (SAR) with a wind scatterometer (ESCAT). Additional payload elements included a radar altimeter, along-track scanning radiometer, precise range and range-rate equipment, and a laser retro-reflector. Originally designed for a nominal lifetime of three years, ERS-1 significantly exceeded expectations, operating successfully until March 2000. The mission concluded after nearly nine years of service following a failure in the spacecraft's attitude control system. The ERS-2 satellite, launched on 21 April 1995, served as a follow-on mission. It carried an almost identical payload to ERS-1, with the addition of an atmospheric ozone sensor. ERS-2 remained operational for 16 years and was decommissioned in July 2011. Together, ERS-1 and ERS-2 established a 20-year global archive of scatterometer backscatter measurements. Both satellites operated in a sun-synchronous orbit with an altitude of approximately 785 km and an inclination of 98.5°. The nominal orbital period was about 100 minutes. The ascending node crossing time was 22:15 local mean time (LMT) for ERS-1 and 22:30 LMT for ERS-2. Each mission employed a 35-day standard orbit repeat cycle, with ERS-1 additionally supporting 3-day and 168-day repeat cycles for specific mission phases. An overview of key mission parameters is provided in Table 3.1.

Mission parameter	**Unit**	**ERS-1**	**ERS-2**
Launch date	–	1991-07-17	1995-04-21
Spacecraft mass	[kg]	2 384	2 516
ESCAT payload mass	[kg]	1 100	1 100
Ground velocity	[km/s]	7	7
LMT at ascending node	–	22:15	22:30
Orbit type	–	sun-synchronous	sun-synchronous
Orbit height	[km]	782–785	782–785
Repeat cycle	[orbits]	43 501 2411	501
	[days]	3 35 168	35
Orbits/day	–	14.333 14.314 14.351	14.314

Table 3.1: ERS-1/2 mission parameter overview

3.2 Instrument description

The Active Microwave Instrument (AMI) formed the core of the ERS payload. It was designed as a multi-mode radar system operating at 5.3 GHz (C-band), integrating the functions of a high-resolution Synthetic Aperture Radar (SAR) and a lower-resolution wind scatterometer (ESCAT) [3]. The AMI supported distinct operational modes: image mode and wave mode for SAR acquisitions, and wind mode for scatterometry. Due to the high power consumption and data rate associated with SAR imaging, image and wind modes were mutually exclusive. However, a wind/wave mode enabled sequential switching between wind and wave modes, allowing for concurrent observations of ocean surface wind and wave fields. In wind mode, AMI functioned as a scatterometer, acquiring backscatter measurements using three fan-beam antennas with vertical polarization (VV). These antennas were oriented as follows:

- **Fore-beam**: 45° forward-looking relative to the satellite ground track,
- **Mid-beam**: 90° right-looking,
- **Aft-beam**: 135° backward-looking.

The three beams illuminated a swath approximately 500 km wide (see Figure 3.1). The scatterometer transmitted rectangular radio frequency (RF) pulses with durations of 130 µs for the fore- and aft-beams and 70 µs for the mid-beam. The three antennas were operated in a repeating sequence of 32 RF pulses per beam, starting with the fore-beam. The pulse repetition frequency (PRF) was set to 98 Hz for the fore- and aft-beams, and 115 Hz for the mid-beam, resulting in a full cycle, referred to as an FMA sequence, lasting 940.84 ms. Four consecutive FMA sequences corresponded to 3.763 s, covering approximately 25 km along the satellite ground track. Within each 32-pulse sequence per beam:

- **4 internal calibration pulses** were recorded. These pulses were replicas of the transmitted signal, routed through the receiver chain to monitor transmit power and receiver gain, ensuring instrument stability throughout the mission.
- **28 noise measurements** were acquired to characterize system noise, accounting for thermal background radiation and improving the signal-to-noise ratio of the backscatter signal.

An analog-to-digital converter (ADC) sampled the echo signals, calibration pulses, and noise measurements at 30 kHz. For the mid-beam, this sampling rate translated to an across-track spatial resolution of approximately 32.4 km at an incidence angle of 18°, and 14 km at 45.5° [4]. An overview of the ESCAT technical parameters is provided in Table 3.2.

3.3 Ground processing

The sampled echo signals, internal calibration pulses, and noise measurements were stored onboard using tape recorders following initial onboard processing. These data packages were subsequently downlinked to ground stations, along with supporting data such as orbit and attitude information and relevant instrument parameters, to enable the required system performance through further on-ground processing. The ground processing chain comprised several key steps:

1. **Internal calibration and signal correction:**
   The first processing step aimed to enhance the signal-to-noise ratio (SNR) and correct for fluctuations in the transmitter and receiver chains, using the recorded internal calibration data.
2. **Conversion to normalized radar cross section (σ^0):**
   The processed power echo samples were then converted to the normalized radar cross section (σ^0). This conversion utilized predetermined normalization factors, which represented the power input corresponding to a reference backscatter coefficient of unity at the Earth's surface. The normalization factors were geometry-dependent and provided as look-up tables (LUTs) for each antenna

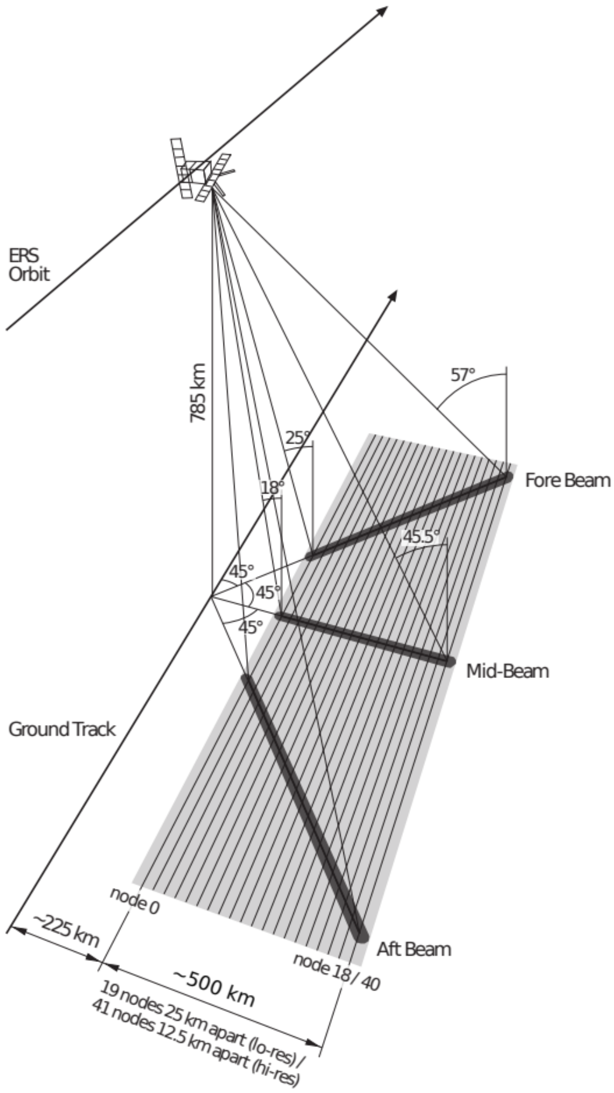

Figure 3.1: Geometrical instrument configuration and resulting orbit grid representation of ERS ESCAT. (Figure adapted from [5]).

beam along the orbit.

3. **Spatial filtering and gridding:**
   To improve radiometric resolution and achieve the desired point target response, a spatial filter was applied to the σ^0 samples. The resulting values were mapped onto a predefined grid of nodes covering the entire swath:

   - The central node of the swath was defined by the intersection of the mid-beam boresight with the Earth's surface.
   - Additional nodes were placed at 25 km intervals in the across-track direction, extending from the central node toward the swath edges, along a line perpendicular to the satellite ground track.
   - This process was repeated every four FMA sequences ($\sim$3.763 s), corresponding to an along-

Instrument parameter	**Unit**			**Value**
Frequency	[GHz]			5.3
Wavelength	[cm]			5.66
Band	–			C-band
Polarization	–			VV
Swath width	[km]			500
Swath offset	[km]			200
Beam resolution	–			Range gate
Spatial resolution	[km]			25/50
Radiometric resolution	[%]			6.5–7
Dynamic range	[dB]			42
Detection bandwidth	[kHz]			25
Peak power pulse	[W]			4800
Number of pulses per 50 km	–			256
		fore	**mid**	**aft**
Incidence angle	[deg]	25–59	18–47	25–59
Antenna angle	[deg]	45	0	−45
Antenna length	[m]	3.6	2.5	3.6
Pulse duration	[µs]	130	70	130
Pulse repetition interval	[ms]	10.21	8.70	10.21
PRF	[Hz]	98	115	98
Return echo window duration	[ms]	3.93	2.46	3.93
Sampling rate	[kHz]	30	30	30
Number of bits for I/Q	–	8	8	8
Number of samples – Echo signal	–	118	74	118
Number of samples – Calibration pulse	–	30	30	30
Number of samples – Noise	–	32	32	32

Table 3.2: ESCAT technical parameter overview

track node spacing of 25 km.

4. **Weighted averaging using a Hamming function:**
   For each antenna beam, σ^0 samples within a defined area around each node were averaged in both along-track and across-track directions. A Hamming function was used to apply weights to the σ^0 samples based on their distance from the target node. This step was critical, as it influenced both the characteristics of the resulting σ^0 values and the effective spatial resolution of the final product.

The final output of this processing stage was a set of σ^0 triplets – one σ^0 value per antenna beam, assigned to each node in the swath. A detailed description of the ERS-1/2 ESCAT ground processing chain is provided in [4] and [6].

4 Retrieval of backscatter observables

4.1 Pre-processing

The retrieval algorithm described in the following sections is based on the high-resolution ERS-2 Scatterometer Level 2.0 products (`ERS.ASPS20.H`), developed in ESA's SCIRoCCo project from 2014 to 2017. These products serve as the primary input for deriving the FDR4LDYN data records.

1. In the first step, the scatterometer observations were spatially resampled to a fixed Earth grid using a nearest-neighbor approach. The target grid is a Fibonacci grid with a spatial sampling distance of 12.5 km, chosen for its favorable geometric properties and consistency with existing ASCAT products. Figure 4.1 provides a graphical depiction of this grid sampling scheme.

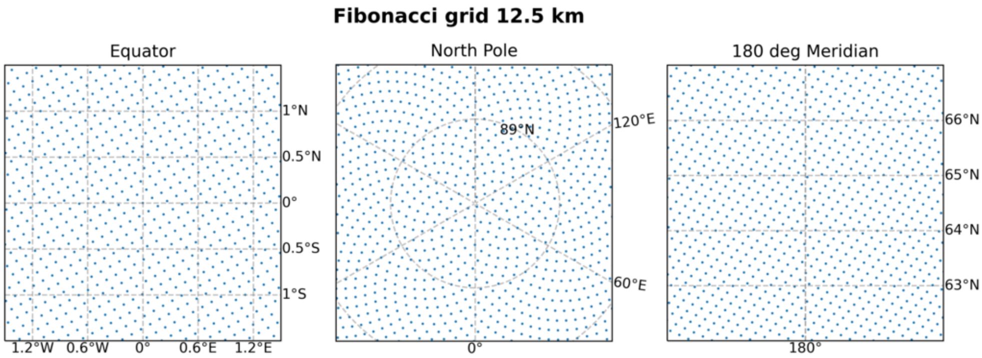

Figure 4.1: Fibonacci grid with 12.5 km sampling (N=1,650,000) showcasing 3 different areas: Equator (left), North Pole (center), and 180° meridian.

2. Following resampling, a comprehensive quality assessment of the ERS-1 and ERS-2 data records was conducted. The analysis addressed data quality flags, spatial and temporal sampling characteristics, outlier detection, break and trend identification, and cross-calibration between ERS-1 and ERS-2. A detailed discussion of the outcomes of this assessment is provided in the dedicated Quality Assessment, Quality Control, and ASCAT Interoperability Report [7].

3. In addition, synthetic ESCAT datasets were generated by temporally sub-sampling ASCAT data to match the lower observation density of the ERS missions. To further align with ESCAT measurement characteristics, only right-swath observations were retained, and measurements outside ESCAT's incidence angle range were excluded. These experiments helped to identify necessary adaptations in the retrieval of backscatter-derived observables when working with sparser sampling. Insights from this analysis informed the design of the final FDR4LDYN data processing chain. A detailed discussion of these analyses is also provided in [7].

4. Based on these results, quality control measures were implemented. Measurements of compromised quality were filtered using the available instrument flags, as detailed in Table 4.1. In addition, extreme outliers, defined as values exceeding $2.5\times$ inter-quartile range $(\mathrm{Q3} - \mathrm{Q1})$, corresponding to $\approx 3.4\sigma$ under a normal distribution, were masked. Specific algorithmic adaptations to the processing steps based on the synthetic experiment will be detailed in the following sections.

Node Confidence Data 1 Flag	Flag meaning
Bit 3: Fore beam flag	no fore beam calculation
Bit 4: Mid beam flag	no mid beam calculation
Bit 5: Aft beam flag	no aft beam calculation
Bit 6: Doppler compensation CoG flag (fore)	compensation out of the defined interval
Bit 7: Doppler compensation StDev flag (fore)	compensation out of the defined interval
Bit 8: Doppler compensation CoG flag (mid)	compensation out of the defined interval
Bit 9: Doppler compensation StDev flag (mid)	compensation out of the defined interval
Bit 10: Doppler compensation CoG flag (aft)	compensation out of the defined interval
Bit 11: Doppler compensation StDev flag (aft)	compensation out of the defined interval
Bit 12: Doppler frequency Shift (fore)	frequency shift out of the defined interval
Bit 13: Doppler frequency Shift (mid)	frequency shift out of the defined interval
Bit 14: Doppler frequency Shift (aft)	frequency shift out of the defined interval
Bit 15: Yaw error angle flag	yaw error out of the defined interval
Bit 16: Frame checksum flag	any beam above or equal to the defined thresholds
Node Confidence Data 2 Flag	**Flag meaning**
Bit 3: Internal calibration flag	any beam above or below the defined thresholds
Bit 4: Arcing flag (fore)	at least 1 arcing detected on fore beam
Bit 5: Arcing flag (mid)	at least 1 arcing detected on mid beam
Bit 6: Arcing flag (aft)	at least 1 arcing detected on aft beam
Bit 7: Noise power flag	any beam above or below the defined thresholds
Bit 8: Limit of kp value	any beam above or below the defined thresholds
Geophysical PCD	**Flag meaning**
Bit 1: Land-sea flag	sea

Table 4.1: Instrument flags applied from `ERS.ASPS20.H` input data

4.2 Inter-calibration of sensor beams to Metop-A ASCAT

To ensure data continuity and facilitate the creation of a long-term backscatter record, the ERS backscatter measurements are inter-calibrated to the Metop-A ASCAT reference as a first main processing step. The processing follows the rainforest-based inter-calibration approach of [8], as practically implemented and adapted for the complete ASPS-reprocessed ERS data record by [9]. The method adjusts the relative backscatter levels between ERS-1, ERS-2, and Metop-A ASCAT by deriving incidence-angle-dependent correction functions from stable tropical rainforest targets. These targets are used to calculate reference backscatter functions, expressed as backscatter as a function of incidence angle, for each sensor and target region. Inter-calibration coefficients are then derived by linearly modeling the difference between the ERS backscatter measurements and the Metop-A ASCAT reference as a function of incidence angle. These coefficients quantify the necessary adjustments to align the ERS backscatter measurements with the Metop-A ASCAT reference. To ensure geometric consistency with the single right-swath configuration of ESCAT, only right-swath Metop-A ASCAT observations are used for the inter-calibration.

While [8] also includes a temporal intra-calibration step to correct potential drift and breaks within the ERS data, this step was tested but not applied in the final FDR4LDYN processing. The ASPS-reprocessed ERS observations showed good temporal stability over rainforest targets during gyroscopically stable mission periods, with estimated instabilities not exceeding approximately $0.033\,\mathrm{dB}$. Moreover, the derived intra-calibration parameters could not be unambiguously attributed to true instrumental changes rather than subtle geophysical variability. Applying them would therefore introduce a risk of overcorrection.

For ERS-2, the gyroscope failure and subsequent tape-recorder degradation further limit the availability of stable rainforest observations, especially over the Amazon and Congo regions after 2003. Consequently, robust intra-calibration coefficients cannot be derived for large parts of the late ERS-2 record using the original methodology. Therefore, to preserve the integrity of potential long-term vegetation dynamics signals within the ERS data and avoid unnecessary manipulation, we apply only a single set of inter-calibration parameters for the entire time period of each ERS mission, ERS-1 and ERS-2.

4.2.1 Selection of natural calibration targets

Calibration is performed using data collected over portions of tropical rainforests that show exceptional long-term stability, as well as azimuthal isotropy and spatial homogeneity of backscatter measurements. Candidate calibration targets are selected according to three criteria: low azimuthal anisotropy, low temporal variability, and high spatial homogeneity of normalized backscatter. The applied thresholds are $\delta < 0.3\,\mathrm{dB}$ for ERS and $\delta < 0.2\,\mathrm{dB}$ for Metop-A ASCAT, temporal variability below $0.4\,\mathrm{dB}$, and spatial backscatter variability below $0.15\,\mathrm{dB}$.

In particular, measurements over the Amazon and Congo rainforests formed the basis for the inter-calibration procedure because of their large spatial extent and the high number of stable grid points available for robust parameter estimation. Additional rainforest regions in Upper Guinea and Southeast Asia are used as independent validation regions to assess the transferability of the derived calibration parameters. More details on the selection parameters and the extent of the selected regions can be found in [9] and in the dedicated Quality Assessment, Quality Control, and ASCAT Interoperability Report [7].

4.2.2 Calculation of reference polynomials

First, a stable one-year period was chosen for each satellite (Table 4.2) to serve as its calibration reference. For Metop-A and ERS-2, the years 2007 and 1998, respectively, were selected as calibration reference periods, consistent with the methodology of [8] and [9]. For ERS-1, the period from May 1992 through April 1993 was chosen to ensure a full year of stable mission phase, as the ERS-1 mission underwent several phase changes during its operational period.

Table 4.2: Reference periods for backscatter calibration of ERS-1 and ERS-2 to Metop-A.

Satellite	Reference period
ERS-1	1992-05-01 - 1993-04-30
ERS-2	1998-01-01 - 1998-12-31
Metop-A	2007-01-01 - 2007-12-31

Second, for each target region, backscatter measurements were normalized to $40°$ incidence angle on a monthly basis using Equation 1 in order to facilitate comparisons across diverse viewing geometries.

$$\sigma^0(L, t_i, 40^\circ, \phi_j) = \sigma^0(L, t_i, \theta, \phi_j) - B_1(L, 40^\circ, \phi_j) \cdot (\theta - 40^\circ) \quad (1)$$

To minimize the influence of seasonal vegetation dynamics on the calibration process, these periodic and predictable effects were removed from the normalized backscatter time series by calculating the mean backscatter value for each day of year across the entire time series, excluding years affected by known instrument anomalies, such as the ERS-2 gyroscope failure and subsequent tape-recorder degradation/failure. These anomalies introduce uncertainties into the backscatter measurements; see [7] and [9] for a detailed discussion of their impact. This seasonal cycle was then subtracted from the backscatter data, and the overall time series mean, excluding the affected years, was added back to preserve the long-term average backscatter level. This step reduces complexity in the calibration process by isolating the stable, long-term backscatter characteristics of the rainforest from seasonal variations.

Next, we characterized measurements from the calibration periods as second-degree polynomials for each satellite, calibration region, and orbit direction, representing the expected stable backscatter response over incidence angle for that region:

$$\overline{\sigma^0}(L_T, \theta) = B_0(L_T, 40°) + B_1(L_T, 40°) \cdot (\theta - 40°) + B_2(L_T, 40°) \cdot (\theta - 40°)^2 \tag{2}$$

where L_T is the target location, e.g. the Amazon or Congo rainforest, θ is the incidence angle, and $\overline{\sigma^0}$ represents the expected σ^0 over the target for a particular incidence angle.

4.2.3 Calculation of inter-calibration coefficients

Prior to calculating the inter-calibration coefficients, several quality control measures were applied to ensure the reliability of the backscatter observations. Only valid triplet measurements, where all three beams had non-null backscatter and incidence angle values and more than 50 echoes, that raised no quality flags were used. For ERS-2, observations affected by known mission anomalies were excluded from the estimation of inter-calibration coefficients. In particular, the coefficients were derived from radiometrically stable parts of the record, excluding observations affected by the gyroscope failure beginning in 2001 and the subsequent tape-recorder degradation/failure from 2003 onward. These periods exhibit increased orbital and sampling irregularities and are therefore not used for calibration parameter estimation. Furthermore, any grid points with fewer than 10 observations were excluded.

To facilitate a reliable comparison between ERS and Metop-A, the analysis considered the different incidence angle ranges for each sensor's beams. The ERS scatterometers' fore- and aft-beams operate with incidence angles ranging from $25°$ to $59°$, while the mid-beam covers a range from $18°$ to $47°$. Metop-A ASCAT's fore- and aft-beams range from $33.7°$ to $64.5°$, and its mid-beam ranges from $25°$ to $53.5°$. For the purpose of calculating calibration parameters, we limited observations from all satellites to those within the overlapping incidence angle ranges of $35°$ to $55°$ for the fore-/aft-beams and $25°$ to $45°$ for the mid-beam. For Metop-A ASCAT, only right-swath observations were retained to maintain geometric consistency with the single-swath ESCAT configuration.

Only common calibration points between the reference and target were examined; in cases of different grid resolutions, the nearest target point to each reference point was selected without duplication.

For each calibration region L_T, we calculated the difference $C_{IES}(L_T, t_i, \theta, \phi_j)$ between each backscatter observation $\sigma^0_{Tar}(L_T, t_i, \theta, \phi_j)$ and the expected backscatter for that observation according to $\overline{\sigma^0_{Ref}}$, which we already determined in Section 4.2.2.

$$C_{IES}(L_T, t_i, \theta, \phi_j) = \overline{\sigma^0_{Ref}}(L_T, t_i, \theta, \phi_j) - \sigma^0_{Tar}(L_T, t_i, \theta, \phi_j) \tag{3}$$

Then we fit a linear model to the differences C_{IES} versus the incidence angle θ for each azimuth configuration ϕ_j, including observations from *all* calibration regions. In this polynomial model (Equation 4), the correction coefficient $C_0(40)$ adjusts the vertical offset, or y-intercept, between corresponding beams of the two satellites, harmonizing their overall backscatter levels at the reference angle of $40°$. Coefficient $C_1(40)$ modifies the slope of each beam's angular response, correcting for differences in sensitivity to incidence angle changes. See Table 4.3 for the parameters of the fit models.

$$\overline{C_{IES}}(\theta, \phi_j) = C_0(40) + C_1(40) \cdot (\theta - 40) \tag{4}$$

Table 4.3: Inter-calibration coefficients for ERS-1 and ERS-2 to Metop-A.

Satellite	**Beam/Orbit**	C_0 **(dB)**	C_1 **(dB/deg)**
ERS-1	Fore/Descending	-0.07083	-0.00900
	Fore/Ascending	0.18181	-0.01445
	Mid/Descending	0.04730	-0.00166
	Mid/Ascending	0.30304	-0.00858
	Aft/Descending	-0.17791	-0.00705
	Aft/Ascending	0.13119	-0.01652
ERS-2	Fore/Descending	0.08373	-0.00914
	Fore/Ascending	0.30394	-0.01489
	Mid/Descending	0.20712	0.00076
	Mid/Ascending	0.42341	-0.00708
	Aft/Descending	0.01713	-0.00813
	Aft/Ascending	0.25110	-0.01800

The derived inter-calibration models were then applied to every backscatter observation in ERS-1 and ERS-2. For each observation, the appropriate model was evaluated based on the sensor, ERS-1 or ERS-2, beam, fore, mid, or aft, orbit direction, ascending or descending, and incidence angle to determine a correction factor in decibels. This correction factor was then added to the original backscatter value to bring the observation into alignment with the Metop-A reference. These corrected backscatter values were then used as input for subsequent processing steps.

The resulting inter-calibration substantially improves the consistency between ERS-1/2 ESCAT and Metop-A ASCAT. Validation over independent rainforest regions shows that the mean residual bias at $40°$ incidence angle is reduced to approximately $0.1\,\mathrm{dB}$, with remaining biases of about $0.12\,\mathrm{dB}$ for ascending orbits and $0.07\,\mathrm{dB}$ for descending orbits. The correction also reduces the incidence-angle dependence of inter-instrument differences and improves beam-to-beam consistency within the ERS instruments.

It should be noted that the inter-calibration is designed to reduce systematic mission-to-mission differences in absolute backscatter level and incidence-angle response. It does not fully resolve all known ERS-2 anomalies after the gyroscope failure and tape-recorder degradation/failure. These periods remain subject to reduced spatial sampling and potentially increased uncertainty, and may require specialized treatment.

4.3 Correction of azimuth angle dependency

The backscatter signal is influenced by both surface properties – such as dielectric characteristics, roughness, and vegetation cover – and the measurement geometry. In particular, the backscattering coefficient varies with the incidence angle θ and the azimuth angle ϕ, the latter describing the orientation of the satellite's line of sight relative to the surface. In certain regions, notably mountainous terrain and sandy deserts, azimuthal effects can be especially pronounced due to directional surface features. These anisotropic scattering behaviors are corrected using a polynomial adjustment to the backscatter signal, following the method proposed by [10].

The azimuth angle under which a location is observed depends on the sensor's beam (fore, mid, or aft) and the satellite's orbit direction (ascending or descending). For ASCAT, there is an additional distinction between the left and right swaths, resulting in 12 unique azimuth configurations (ϕ_i with $i \in [0, 11]$). For ESCAT, which collects data only from the right swath, there are six such configurations (ϕ_i with $i \in [0, 5]$). For each configuration, the incidence angle dependence of backscatter is modeled using a second-order polynomial. These polynomials form the basis for correcting azimuthal anisotropy in the backscatter signal:

$$\sigma_i^0(\theta) = A_i \cdot (\theta - 40)^2 + B_i \cdot (\theta - 40) + C_i \tag{5}$$

Two conditions must be met to compute a polynomial: at least 6 valid measurements must be available, and their incidence-angle range must exceed the threshold of $15°$ for the given geometry.

The coefficients of the six second-order polynomials (A_i, B_i, C_i) are determined by fitting each polynomial to all observations within the corresponding azimuth configuration (e.g., all measurements from the right swath fore beam in ascending orbit). In the current ASCAT processing, an additional global reference model ($i = 12$) is fitted using all available observations across viewing geometries. This model serves as the baseline against which individual azimuth configurations are corrected. Since ESCAT provides only six azimuthal configurations, compared to twelve in ASCAT, a modified strategy is required to ensure consistency across the long-term data record. To harmonize both missions, the reference polynomial has been redefined to rely exclusively on right-swath observations, the geometry consistently available in both ESCAT and ASCAT datasets. Global statistical analyses confirm that polynomial coefficients derived from left- and right-swath data are nearly indistinguishable, with their differences following a near-normal distribution. The only exceptions are regions with pronounced azimuthal anisotropy, notably sand dune deserts and the Greenland ice sheet. Even in these cases, however, adopting either a common reference or a single viewing geometry as a reference effectively reduces azimuthal noise without distorting the underlying geophysical signal. This provides a solid justification for adopting right-swath data as the reference geometry not only for ESCAT but also for future ASCAT and combined ESCAT–ASCAT products.

A more challenging aspect arises when comparing ascending and descending passes. Consistently higher backscatter values are observed in descending orbits – acquired at approximately 10:30 local time (ESCAT) and 09:30 (ASCAT) – relative to ascending orbits, which occur at 22:30 (ESCAT) and 21:30 (ASCAT). At $40°$ incidence angle, the global mean of the difference is approximately 0.25 dB. This offset is most plausibly explained by diurnal variations in soil and vegetation conditions, and thus represents a genuine geophysical signal. Using a single reference polynomial blending ascending and descending passes, as done in the current ASCAT processing, suppresses these diurnal effects, effectively averaging away valuable information. Figures 4.2 and 4.3 present the systematic differences in backscatter at 40° incidence angle, contrasting left versus right swath data and ascending versus descending passes for ASCAT data. The ascending–descending comparison reveals a systematic bias attributable to diurnal effects, whereas the left–right comparison shows no such bias and highlights only regions with pronounced azimuthal anisotropy.

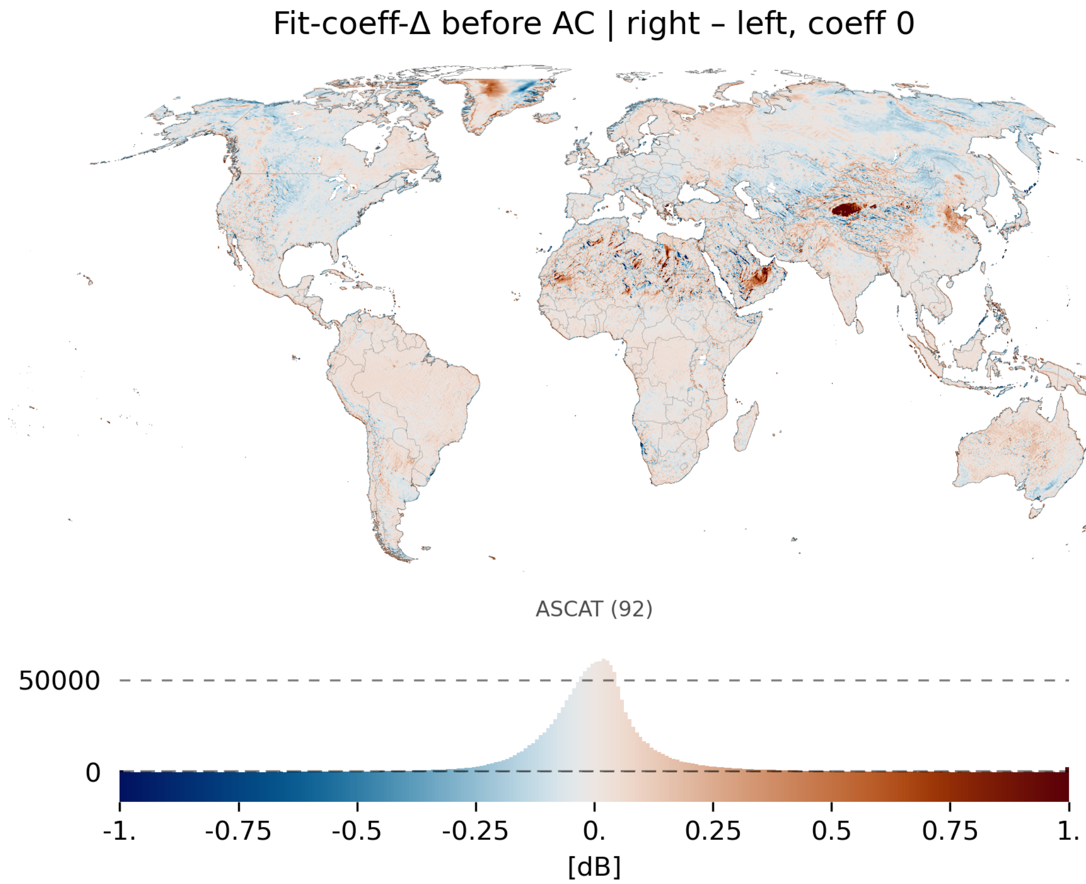

Figure 4.2: Global map of differences in backscatter (dB) at 40° incidence angle between left and right ASCAT data. The values are computed as right minus left, such that positive values (shown in red) indicate higher backscatter in right swath data.

The complication is that ascending–descending differences are not solely due to diurnal processes; they also include azimuthal anisotropy, which is precisely the component targeted for removal in this processing step. For ASCAT, disentanglement of these components might be possible by exploiting viewing geometries with nearly identical azimuth angles across swaths (e.g., left-ascending-fore vs. right-descending-aft), where observed differences are rather attributable to diurnal cycles than to azimuthal effects. ESCAT, however, lacks such symmetry, as it provides only right-swath measurements. Consequently, it is not possible to isolate diurnal and azimuthal contributions with the same rigor. Given this constraint, the algorithmic design in FDR4LDYN prioritizes the retention of the diurnal signal, accepting slightly elevated levels of azimuthal anisotropy in the final dataset. This is operationalized by defining two separate reference polynomials: right-ascending for all ascending viewing directions and right-descending for all descending directions. Instead of a single global reference, the system now employs two orbit-dependent references.

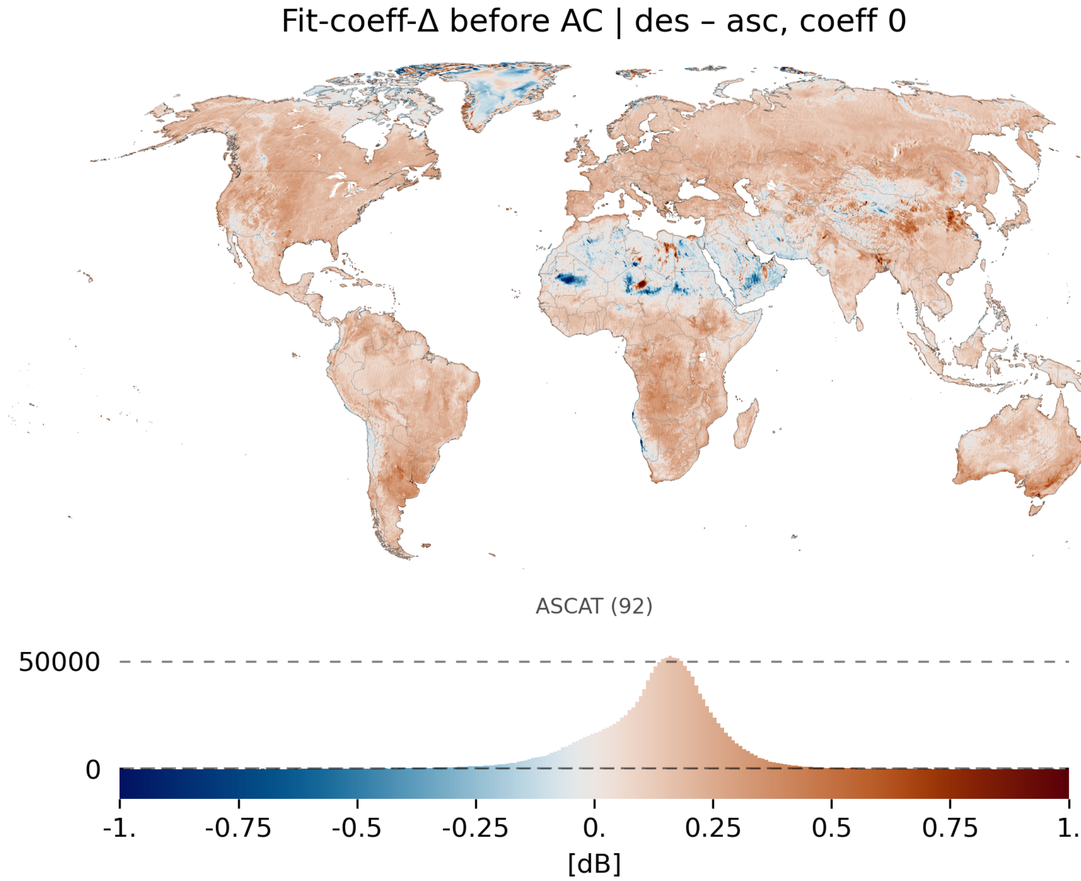

Figure 4.3: Global map of differences in backscatter (dB) at 40° incidence angle between ascending and descending ASCAT data. The values are computed as descending minus ascending, such that positive values (shown in red) indicate higher backscatter in descending (morning) passes.

For ESCAT, this yields a total of $3 \times 6 = 18$ static polynomial coefficients across the six geometric configurations, complemented by an additional $2 \times 3 = 6$ coefficients corresponding to the two reference polynomials. In previous ASCAT processing, the difference between the polynomial of each viewing configuration and the reference was used to apply a static correction to the backscatter signal. However, this approach assumes that the angular scattering behavior of land targets remains stable over long periods – a condition that does not hold in all regions. For example, urban expansion can introduce new directional reflectors (e.g., building edges), and vegetation changes along the margins of arid regions, such as those observed in the Sahel [11], may alter backscatter characteristics over time [10]. To address these limitations, the updated correction method also introduces dynamic reference polynomials. As before, six azimuth configuration subsets are defined. However, in the dynamic approach, a separate second-order polynomial is fitted for each year using an 8-year rolling window (current year $\pm$ 3.5 years). This approach yields a total of 126 sets of polynomial coefficients (6 configurations $\times$ 21 years). These dynamic coefficients are then used in the yearly azimuth normalization procedure. A schematic illustration of the azimuthal correction procedure, using an example for a yearly subset and an incidence angle of 40°, is shown in Figure 4.4.

This way, the individual incidence angle dependencies of backscatter are adjusted to their corresponding reference, mitigating azimuth effects, while retaining diurnal and long-term changes in backscatter

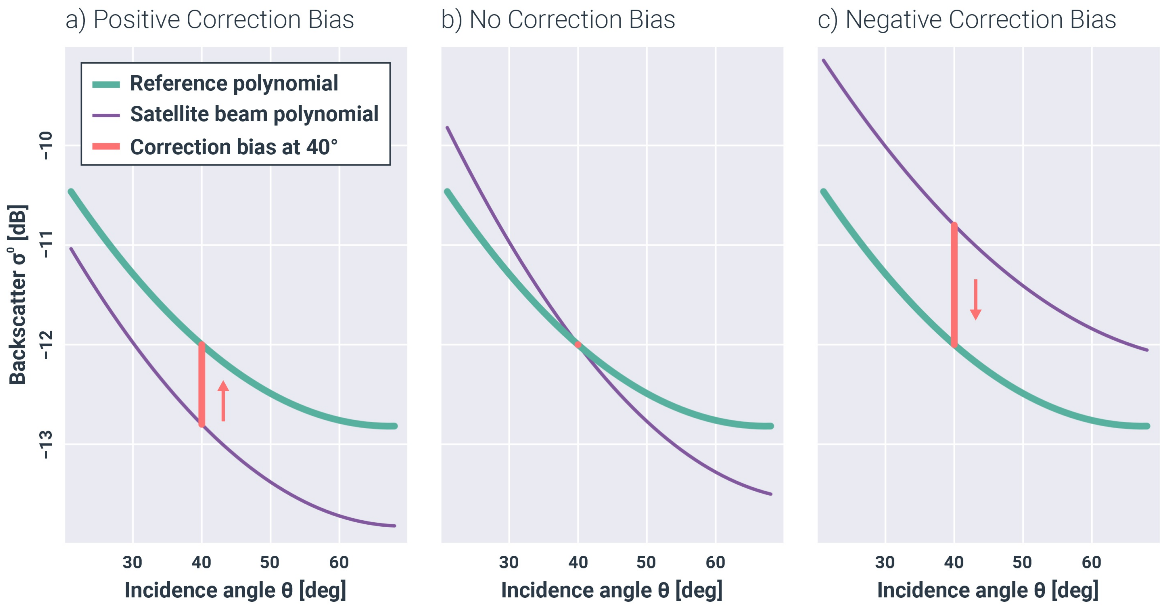

Figure 4.4: Scheme for calculating azimuth correction biases through second-order polynomials for three example geometric configurations, along with their corresponding reference polynomial. The correction bias for a point at a given incidence angle is determined by the difference between these functions and can be positive (a), zero at intersection points (b), or negative (c). This procedure is consistently applied across all six combinations of fore/mid/aft beams, and ascending/descending orbits, and separately for each yearly subset. (Figure from [12]).

behavior:

$$\hat{\sigma}^0_{i,y}(\theta) = \sigma^0_{i,y}(\theta) + (A_{ref,y} - A_{i,y}) \cdot (\theta - 40)^2 + (B_{ref,y} - B_{i,y}) \cdot (\theta - 40) + (C_{ref,y} - C_{i,y}) \quad (6)$$

where $\hat{\sigma}^0_{i,y}$ represents the corrected backscatter for each configuration i and yearly subset y.

The yearly azimuthal correction parameters are distributed as a separate FDR4LDYN product, enabling users to investigate environmental dynamics associated with azimuthal anisotropy, such as wind-driven sand dune migration or ice-sheet evolution.

4.4 Estimated standard deviation (ESD) of backscatter

The Estimated Standard Deviation (ESD) represents a measure of measurement noise in the backscatter signal and is expressed in decibels. The ESD is derived from the fore and aft beam measurements (σ^0_f and σ^0_a) based on the following observation: all three beams observe the same surface target within a short time interval, and the fore and aft beams, in particular, do so at nearly identical incidence angles. Therefore, in the absence of azimuthal effects, the fore and aft measurements are expected to be statistically comparable – that is, drawn from the same underlying distribution. Hence, the expectation of the difference

$$\delta := \mathrm{E}\left[\sigma_f^0 - \sigma_a^0\right] = 0 \tag{7}$$

should be zero, and the variance of this difference can be expressed as twice the variance of one of the beams (i.e $\mathrm{Var}\left[\delta\right] = 2 \cdot \mathrm{Var}\left[\sigma^0\right]$). This can be derived using error propagation and neglecting higher-order terms:

$$\mathrm{Var}\left[\delta\right] \approx \mathrm{Var}\left[\sigma_f^0\right] \cdot \left(\frac{\partial\delta}{\partial\sigma_f^0}\right)^2 + \mathrm{Var}\left[\sigma_a^0\right] \cdot \left(\frac{\partial\delta}{\partial\sigma_a^0}\right)^2 + 2 \cdot \mathrm{Cov}(\sigma_f^0, \sigma_a^0) \cdot \left(\frac{\partial\delta}{\partial\sigma_f^0}\right) \cdot \left(\frac{\partial\delta}{\partial\sigma_a^0}\right) + \ldots,$$

whereby the third term is zero under the assumption of i.i.d. (independent and identically distributed random variables):

$$\mathrm{Var}\left[\delta\right] \approx \mathrm{Var}\left[\sigma_f^0\right] \cdot (1)^2 + \mathrm{Var}\left[\sigma_a^0\right] \cdot (-1)^2 + 0 \tag{8}$$

Assuming equal variances for the fore- and aft-beam, we obtain:

$$\mathrm{Var}\left[\delta\right] \approx \mathrm{Var}\left[\sigma_f^0\right] + \mathrm{Var}\left[\sigma_a^0\right] = 2 \cdot \mathrm{Var}\left[\sigma^0\right] \tag{9}$$

The previous equation can be rewritten to find the final formula for the ESD:

$$\mathrm{ESD}\left[\sigma^0\right] = \sqrt{\frac{\mathrm{Var}\left[\delta\right]}{2}} \tag{10}$$

The ESD is computed after strong outliers (defined as $\delta > Q3 + 3 \times \mathrm{IQR}$ or $\delta < Q1 - 3 \times \mathrm{IQR}$) have been removed.

To capture the temporal evolution of the ESD, this parameter, like azimuthal correction parameters, is calculated both annually and over the entire time series. The yearly ESD values are again provided as a separate FDR4LDYN data record.

4.5 Estimation of slope and curvature

In general, backscatter measurements over land show a strong dependence on the incidence angle, and a linear function (defined in the dB domain) is usually deemed sufficient to describe this relationship. The backscatter coefficient at an arbitrary incidence angle σ^0 (in dB) can be modelled as:

$$\sigma^0\left(\theta\right) = \sigma^0\left(40\right) + \sigma' \cdot \left(\theta - 40\right) \tag{11}$$

where $40°$ is the reference incidence angle, $\sigma^0\left(40\right)$ denotes the backscatter at this reference angle (in dB), and σ' represents the slope of the backscatter–incidence angle relationship (in dB/degree). For most land cover types, this linear approximation is valid due to the characteristic decrease in backscatter with increasing incidence angle. However, in cases where volume scattering becomes significant, such as in vegetated or snow-covered regions, the backscatter curve may flatten or deviate from linearity at higher incidence angles. To capture such non-linear behavior, again a second-order polynomial is introduced, incorporating a curvature term σ'':

$$\sigma^0(\theta) = \sigma^0(40) + \sigma' \cdot (\theta - 40) + \frac{1}{2} \cdot \sigma'' \cdot (\theta - 40)^2 \tag{12}$$

From a mathematical perspective, Equation 12 represents a Taylor polynomial, as it approximates the backscatter function using a finite sum of its derivatives evaluated at a single point. In this case, the reference incidence angle of 40° serves as the expansion point. The first derivative, σ' (in dB/degree), and the second derivative, σ'' (in dB/degree^2), correspond to the slope and curvature of the backscatter–incidence angle relationship at this reference point. Once these parameters are known, the Taylor polynomial can be used to estimate backscatter values at nearby incidence angles. Conversely, by rearranging Equation 12, the backscatter at the reference incidence angle, $\sigma^0(40)$, can be inferred from a measurement taken at an arbitrary incidence angle θ.

Several methods have been developed to estimate σ' and σ'' over time, all of which are based on the concept of local slope computation [13]. A local slope provides an instantaneous estimate of the incidence angle dependency of backscatter, derived from differences in the measured signal across beams. Specifically, $\sigma_f^0 - \sigma_m^0$ and $\sigma_a^0 - \sigma_m^0$ can be used, since the fore and aft beams observe the target at the same incidence angle (i.e., $\theta_f = \theta_a$):

$$\sigma'_{fm} = \frac{\sigma_m^0 - \sigma_f^0}{\theta_m - \theta_f}, \quad \sigma'_{am} = \frac{\sigma_m^0 - \sigma_a^0}{\theta_m - \theta_a} \tag{13}$$

where σ'_{fm} and σ'_{am} represent slope estimates at the local incidence angle midpoints between the mid and fore beams, and the mid and aft beams, respectively:

$$\theta_{fm} = \frac{\theta_m + \theta_f}{2}, \quad \theta_{am} = \frac{\theta_m + \theta_a}{2} \tag{14}$$

If a sufficiently large and well-distributed sample of local slope estimates is available across the full range of incidence angles, a first-order approximation of $\sigma'(\theta)$ can be used to estimate the slope σ' and curvature σ'' at 40° via linear regression:

$$\sigma'(\theta) = \sigma' + \sigma'' \cdot (\theta - 40) \tag{15}$$

4.5.1 Kernel smoother method

The selection and weighting of local slope values used in the regression model have evolved over time, influenced by both data availability and computational considerations. A detailed overview of past implementations can be found in [13]. The approach to estimating σ' and σ'' currently being used in ASCAT processing is based on a Kernel Smoother (KS) method [14]. This implementation allows slope and curvature parameters to be estimated either as a climatology (i.e., one value per day of year, totaling 366 values) or as a daily time series.

For the climatology, regression coefficients are computed for each day of year d_0 by selecting local slope values from all years within a symmetric time window of ± 21 days around d_0, resulting in a total kernel width of $\lambda = 42$ days. In contrast, for the dynamic time series-based estimation of slope and curvature, insights from the synthetic ESCAT experiment described in Section 4.1 revealed the need for a wider time window in data-sparse regions and periods, particularly after the ERS-2 tape recorder failure. Unlike the climatology approach, which draws from multiple years, the dynamic method is restricted to observations within the time window of the given date alone. This limitation reduces data availability and makes the method more sensitive to temporal gaps. The narrower ± 21-day window for dynamic slope and curvature used in ASCAT processing was found to introduce noisy estimates, frequent data gaps, and strong edge effects in such conditions in the case of ESCAT data. To mitigate these issues, we adopted a wider window of ± 42 days (i.e., $\lambda = 84$ days) for ESCAT, improving temporal robustness in sparse periods. A detailed account of the experiments with synthetic ESCAT data substantiating these design choices is provided in [7].

For simplicity, the following description focuses on the climatology-based computation. The dynamic estimation follows the same principle but is applied to each individual day in the measurement time series rather than to a fixed day-of-year. It uses only data within the time window centered on the specific date, rather than drawing from all available years.

Within the selected time window, local slope values are weighted according to their temporal distance from d_0 using the Epanechnikov kernel function (see [15], Chapter 6 and Figure 4.5):

$$k(d_0, d) = D\left(\frac{d - d_0}{\lambda}\right) \tag{16}$$

with

$$D(t) = \begin{cases} \frac{3}{4} \cdot (1 - t^2) & \text{if } |t| \leq 1 \\ 0 & \text{else} \end{cases} \tag{17}$$

The Epanechnikov kernel has finite support over the interval $[-\lambda, \lambda]$ and is normalized to integrate to one. The kernel width λ is a key parameter that controls the balance between bias and variance in the estimate: increasing λ reduces the variance by incorporating more observations but simultaneously increases the bias due to the inclusion of more distant (and potentially less representative) data points.

Typically, a kernel function is defined over the independent variable – in this case, the incidence angle θ. However, since the goal here is to estimate the coefficients of the linear approximation (Equation 15) across the full incidence angle range for a specific day of year d_0, the kernel is instead defined over time. More precisely, it acts as a function of the day of year. All local slope values falling within the interval $|(d - d_0)/\lambda| \leq 1$ are included in the weighted linear regression and are weighted based on their temporal distance to d_0, as defined by the Epanechnikov kernel (see Equation 18).

Let $\mathbf{x} \in \mathbb{R}^N$ and $\mathbf{y} \in \mathbb{R}^N$ denote the vectors containing the incidence angles θ_l and corresponding local slope values σ'_l for all N observations within the kernel support around day d_0. Define the design matrix

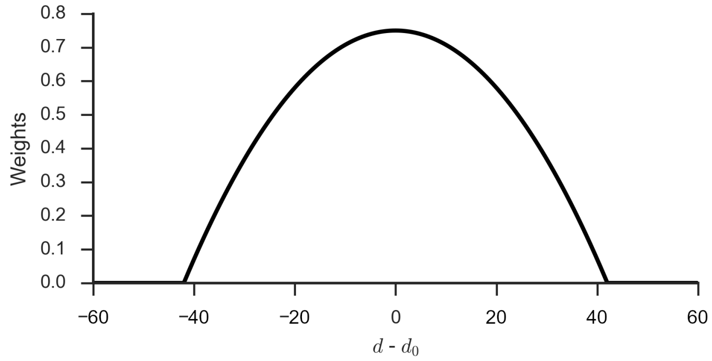

Figure 4.5: Example of the Epanechnikov kernel (λ = 42).

$\mathbf{A} \in \mathbb{R}^{N\times 2}$ such that its first column consists of ones and its second column corresponds to $\mathbf{x}$. Let $\mathbf{W}(d_0) \in \mathbb{R}^{N\times N}$ be a diagonal weight matrix, where the i-th diagonal entry is given by the kernel weight for the i-th observation, i.e., $\mathbf{W}(d_0)[i,i] = k(d_0, d_i)$. Then, the estimates for σ' and σ'' at day d_0 are obtained as:

$$\begin{pmatrix} \sigma'(d_0) \\ \sigma''(d_0) \end{pmatrix} = (\mathbf{A}^T\mathbf{W}(d_0)\mathbf{A})^{-1}\mathbf{A}^T\mathbf{W}(d_0)\mathbf{y} = \mathbf{B}\mathbf{y} \tag{18}$$

If the error covariance of the local slope values used in the fit is given by $\mathbf{\Sigma_l}$, then the error covariance of the parameters is given by:

$$\mathbf{\Sigma}_{\sigma',\sigma''} = \mathbf{B}\mathbf{\Sigma_l}\mathbf{B}^T \tag{19}$$

At the moment, it is assumed that $\mathbf{\Sigma_l}$ is homeoscedastic (i.e., the errors for all local slope values have the same variance s_l^2) and the errors are uncorrelated: $\mathbf{\Sigma_l} = \mathbf{I}s_l^2$, and estimate s_l^2 from the residuals of the fit (in order to avoid confusion with σ for the representation of backscatter, the variance notation is s^2).

Both climatologies and dynamic slopes and curvatures are included in the main FDR4LDYN data record, enabling users to select the most suitable representation for their application. Dynamic slopes and curvatures are particularly valuable for time-sensitive studies such as vegetation dynamics, where the actual temporal evolution of the incidence angle–backscatter relationship is essential. Additionally, they are used in the normalization of backscatter to a reference incidence angle, as described in Section 4.6. Climatologies, by contrast, are sufficient when the mean annual cycle at a location is adequate, for example in the derivation of dry and wet references for surface soil moisture retrieval.

A preliminary inspection of the dynamic slope and curvature estimates derived with the 42-day half-window Epanechnikov kernel revealed occasional strong outliers associated with high noise levels. A detailed analysis showed that these cases occurred when the weighted regression was based on too few local slope estimates or, more critically, when the available local slopes covered only a narrow incidence angle range. In some cases, slopes were derived from measurements acquired at nearly identical incidence angles or over a span of only a few degrees. Such fits are not sufficiently constrained and can lead to unreliable estimates of σ' and σ''. If these dynamic parameters are subsequently used to normalize backscatter to $40°$, the outliers can propagate into the normalized backscatter record and affect downstream applications. To mitigate this issue, the quality criteria for dynamic slope and curvature estimation were strengthened. Each fit must now include at least 6 local slope estimates, instead of the previous mathematically constrained minimum of 4, and these estimates must span an incidence angle range of at least $15°$, i.e., $\max(\theta_l) - \min(\theta_l) \geq 15°$. This additional criterion is consistent with the requirements used in the azimuthal correction procedure. If either condition is not met, no dynamic slope or curvature estimate is provided for the corresponding day, and a dedicated quality flag is set to inform users that the estimate was withheld because the local slope fit was insufficiently constrained.

4.5.2 Regularization method

In addition to the kernel smoother approach, a regularization-based method was developed to better represent the dynamics of slope and curvature at short time scales [16]. To estimate slope and curvature using the regularization method, the same local slopes (Equation 13) and local incidence angles (Equation 14) are used as in the kernel smoother method. All available values of the local slopes and incidence angles are used in one single estimation for each grid point. Instead of applying weights to the observations, the first differences of the estimated slope and curvature time series are constrained by including a first difference matrix ($\mathbf{C}$) and a scalar driving the magnitude of the constraint (γ) in the estimation equation. The equation to estimate the full time series of slope (σ') and curvature (σ'') per grid point becomes:

$$\begin{pmatrix} \sigma' \\ \sigma'' \end{pmatrix} = (\mathbf{A}^T\mathbf{A} + \gamma^2\mathbf{C}^T\mathbf{C})^{-1}\mathbf{A}^T\mathbf{y} \tag{20}$$

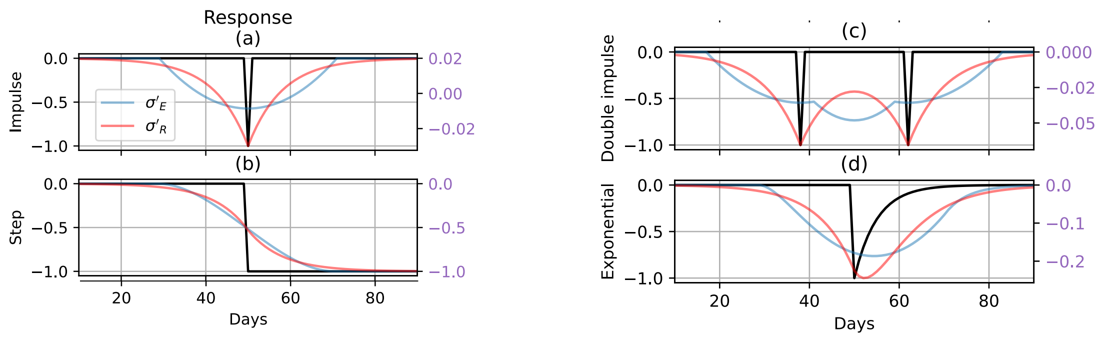

Figure 4.6: Response of kernel smoother (blue) and regularization method (red) to an impulse shown in black: single impulse (a), step (b), double impulse (c) functions, and a step followed by an exponential decay (d). The regularization response is computed with $\gamma = 8$, and the kernel smoother response is computed with a 21-day half-width. Purple axes correspond to the values of the regularization and Epanechnikov responses. Black axes denote the values of the input functions. Figure adapted from [16].

Applying a constraint on the dynamics of the estimated time series, instead of a kernel-based approach, results in a better correspondence between the timing of changes in the observations, and timing of changes in the estimated parameters. Figure 4.6 illustrates the difference between the responses of the kernel smoother and the regularization method to a simplified input signal. The timing of the changes in the regularized time series shows a better correspondence to the changes in the input signal. A more elaborate description and comparison of the estimation method can be found in [16].

4.5.3 Hierarchical Bayes

In this section, we describe a post-processing approach based on *Hierarchical Bayes* methods (HB) to improve already computed dynamic slope and curvature estimates. HB is, in general, used for estimating simultaneously a set of global hyper-parameters that determine the distributions of several related groups, and the parameters for the individual groups. It combines aspects of pooling/shrinking approaches and ANOVA in classical statistics. See, e.g.[17], [18].

In our case, the group level parameters are the dynamic slope values $\sigma'(d,q)$ for a given day d and sensor q combination, including their standard errors, as provided by one of the approaches discussed above (analogously for the curvature), while the hyper-parameters determine the climatology $\mu(doy)$ and and its standard deviation $\tau(doy)$, which governs the amount of shrinkage towards the climatology. The approach discussed below has to be computed for each day of year (doy).

HB could be applied in two scenarios. The first is the fusion of slope estimates across different sensors; this would allow, for example, to fill in (impute) temporal gaps in ESD-based slopes with ASCAT-based slopes; however, this requires temporal overlap and very good inter-sensor calibration.

The second scenario is the simultaneous computation of the climatology and adjustments to the dynamic slopes towards the climatology (intra-annual mean), based on their relative standard errors. This will also fill data gaps and move dynamic slope estimates with high standard error (typically resulting from a low number of observations/local slopes) more strongly towards the climatology. This is illustrated in Figure 4.7.

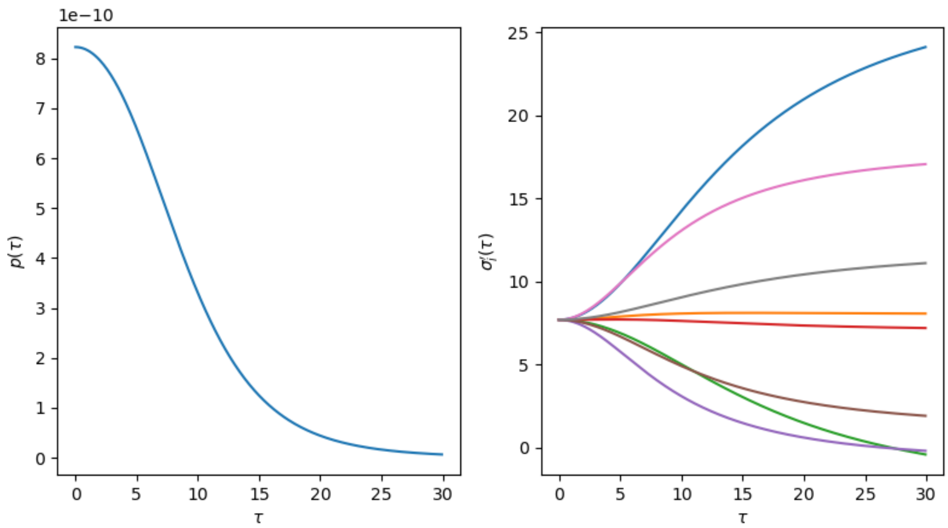

Figure 4.7: **Left:** Inferred posterior probability density function for τ with maximum at 0 (full shrinkage towards the mean). **Right:** Adjusted group means σ'_i (daily dynamic slopes for the same doy, but different years i) as a function of τ. For the maximum likelihood estimate $\tau = 0$, all group means are shrunk towards the (weighted) global mean $\mu(\tau)$ (here: 7.8), for increasing τ, they move towards their original values. Figure adapted and reproduced from the SAT example in [17], section 5.5.

A fully Bayesian treatment requires the marginalization (computation of the expectation by weighting with the p.d.f. and integrating over the domain of the variable) over all hyper-parameters. In the above example, we have marginalized over the posterior distribution for μ, but not for τ, so the group means are still functions of τ. The last integration could be performed either via Markov Chain Monte Carlo algorithms, or we could replace τ by the maximum of its posterior density. The second approach, known as *Empirical Bayes*, is cheaper computationally, but can lead to suboptimal results. For example, in Figure 4.7, right, for $\tau = 0$, all dynamic slopes would be replaced by the global mean (climatology), although it is obvious that there exists a considerable spread between the yearly (dynamic) slope values.

The above example is based on assumed normal distributions for the observations, the group means, and the conditional distribution of $\mu|\tau$, which allows for an analytic solution (except for the marginalization w.r.t τ). If one is prepared to accept a higher computational burden, more complex distributions can be used. It is also possible to extend the approach to regression, e.g., in order to deal with temporal trends in the slopes.

Slopes and curvatures derived from the HB method, as well as from the regularization approach described in Section 4.5.2, will be included in a future extension of the FDR4LDYN product suite. They will be distributed as dedicated data records together with descriptive flags providing quality information.

4.6 Interpolation to reference incidence angle

Once $\sigma'(d)$ and $\sigma''(d)$ have been computed on a daily basis d, the incidence angle interpolation can be applied to the backscatter measurements of each beam b (fore, mid, aft) using:

$$\sigma_b^0(40) = \sigma_b^0(\theta_b) - \sigma'(d) \cdot \Delta\theta_b - \frac{1}{2} \cdot \sigma''(d) \cdot \Delta\theta_b^2 \tag{21}$$

with $\Delta\theta_b = \theta_b - 40$. The backscatter observations of the three beams interpolated to a common reference angle are averaged:

$$\bar{\sigma}^0(40) = \frac{1}{3} \cdot \sum_{b \in \{f,m,a\}} \sigma_b^0(40) \tag{22}$$

which gives the final backscatter $\bar{\sigma}^0(40)$ interpolated at the reference incidence angle. The noise variance of the interpolated backscatter at the reference incidence angle for each beam b is given by:

$$\mathrm{Var}\left[\sigma_b^0(40)\right] = \mathrm{ESD}\left[\sigma^0\right]^2 + \mathrm{Var}\left[\sigma'(d)\right] \cdot \Delta\theta_b^2 + \frac{1}{4} \cdot \mathrm{Var}\left[\sigma''(d)\right] \cdot \Delta\theta_b^4 \tag{23}$$

and after averaging, the noise variance reduces to:

$$\mathrm{Var}\left[\bar{\sigma}^0(40)\right] = \frac{1}{9} \cdot \sum_{b \in \{f,m,a\}} \mathrm{Var}\left[\sigma_b^0(40)\right] \tag{24}$$

In this version of the FDR4LDYN products, dynamic slopes and curvatures obtained using the kernel smoother method (Section 4.5.1) are employed for backscatter interpolation.

4.7 Known signal characteristics and contextual factors

The FDR4LDYN data records provide consistent, calibrated backscatter, slope, and curvature observations over global land surfaces. However, the backscatter signal is inherently influenced by a range of geophysical and observational factors, particularly in complex environments such as dense forests, snow-covered or frozen soils, open water bodies, wetlands, and urban areas. In these cases, the signal may exhibit behaviors that differ from typical land surface scattering and may require careful interpretation. While these effects do not compromise the integrity of the backscatter observations themselves, they can affect the stability and interpretability of derived downstream variables. Users are therefore encouraged to consider ancillary datasets when analyzing time series in such regions. Additionally, the dynamic nature of azimuthal anisotropy, subsurface scattering, and seasonal transitions should be taken into account when assessing temporal changes. These considerations are particularly relevant for applications that use FDR4LDYN products as input to further retrieval algorithms, including soil moisture estimation or vegetation dynamics monitoring. To support informed data use, the FDR4LDYN data records provide a comprehensive set of quality flags that guide users in identifying observations of suitable reliability for their applications.

4.7.1 Vegetation

In densely vegetated regions, such as tropical rainforests, C-band microwaves are largely attenuated by the canopy and do not reach the soil surface. As a result, the backscatter signal carries little to no soil information and typically exhibits very low temporal variability, reflecting limited signal sensitivity to changes in surface conditions.

4.7.2 Desert areas

Desert regions are defined by extremely low soil moisture levels, driven by minimal annual precipitation. As a result, the backscatter signal in these areas is typically weak and exhibits limited temporal variability. In particular, sandy deserts can show backscatter values below -20 dB. These environments are also more susceptible to azimuthal anisotropy and Bragg scattering effects [19]. The latter arises from small-scale surface ripples on sand dunes, which can enhance the backscatter signal for specific incidence angle ranges due to coherent scattering mechanisms. Such effects may introduce directional biases and should be considered when interpreting backscatter, slope, and curvature in arid landscapes.

4.7.3 Subsurface scattering

In arid regions, particularly where soils are very dry, subsurface volume scattering can become a dominant component of the backscatter signal. Under such conditions, the penetration depth of C-band microwaves can reach up to several meters, increasing the likelihood of interactions with buried layers such as bedrock. This phenomenon is especially notable in parts of North Africa, where it can lead to an inverse relationship between backscatter and surface soil moisture. During dry periods, the signal may originate from deeper, reflective subsurface layers, resulting in unexpectedly high backscatter values despite a dry surface. Conversely, during wet periods, the increased surface moisture reduces the penetration depth, limiting the signal's interaction with deeper layers and thus lowering the backscatter. This effect can confound soil moisture retrieval algorithms, which may falsely interpret increasing backscatter during dry-down as a rise in surface moisture [20]. While such misinterpretations are not relevant for the FDR4LDYN product series itself, they should be considered when using the dataset as input for downstream applications. To support this, a subsurface scattering probability flag, developed by [21], is provided as reference. This flag is currently derived from ASCAT data and will be recalculated from ESCAT observations in a future update within the FDR4LDYN project.

4.7.4 Snow

The backscatter signal in snow-covered regions is influenced by a range of snowpack properties, including liquid water content, grain size and shape, snow depth and layering, as well as the roughness of the air–snow interface. Depending on these factors, different scattering mechanisms may dominate, such as surface scattering, volume scattering within the snowpack, or reflection from the underlying soil surface if penetration is sufficient. These complex interactions often reduce the interpretability of the backscatter signal during snow-covered periods. To support the identification of such conditions, a static snow cover probability flag is provided. This flag is derived from auxiliary land surface model data provided by the ERA5-Land reanalysis [22] and enables users to mask time periods likely affected by snow cover. In a future update, a dynamic snow cover flag based on the actual ERA5-Land snow depth history will be employed as part of the FDR4LDYN product suite.

4.7.5 Frozen soil

When soil temperatures fall below 0°C, the dielectric properties of the soil change significantly. As the water in the soil freezes, its molecules can no longer respond to the incoming microwave signal, leading to a marked reduction in backscatter. This freezing effect complicates interpretation, particularly in vegetated areas where plant structures may adapt to cold conditions and partially mask or alter the signal response. To help mitigate these effects, the FDR4LDYN products also include a static frozen soil probability flag, based on ERA5-Land temperature data. In the future, a dynamic flag is also planned in this case. Users are advised to apply this flag to exclude periods where frozen conditions may impair the reliability of the backscatter signal, depending on their desired application.

4.7.6 Surface water and wetlands

In areas with surface water or wetlands, the backscatter signal is primarily governed by surface roughness, as C-band microwaves penetrate only the uppermost 1–2 mm of the water surface. Calm, open water behaves like a specular reflector, directing most of the incoming energy away from the satellite sensor and resulting in very low backscatter values. When surface winds generate small waves, the roughness increases, leading to enhanced backscatter in the upwind and downwind viewing directions, while the signal remains low in crosswind directions. This anisotropic behavior should be considered when interpreting backscatter measurements over water bodies and inundated areas, especially in the context of wind-induced variability or seasonal flooding. A dedicated static flag indicates the fraction of wetlands at each location and can be applied for masking purposes.

4.7.7 Topographic complexity

In mountainous and topographically complex regions, backscatter signals often exhibit high spatial and temporal variability. This variability arises from local differences in slope, aspect, and elevation, which affect the incidence angle and scattering geometry of the microwave signal. Since the FDR4LDYN retrieval algorithm does not explicitly account for terrain-induced effects, users should interpret backscatter, slope, and curvature values in such areas with caution. A static flag also quantifies topographic complexity (in percent), which can be used for masking.

4.7.8 Urban areas

In urban and suburban regions, the backscatter signal may be strongly affected by built structures and heterogeneous land cover. Buildings and other man-made features can introduce distinct scattering mechanisms, such as double or multiple reflections between vertical and horizontal surfaces. These effects are highly directional and can result in unusually high backscatter in specific viewing geometries. Even at the coarse spatial resolution of ESCAT, strong responses from isolated point-like targets can dominate the footprint-level signal [10]. As a result, urban areas may exhibit sharp backscatter peaks and increased anisotropy, which should be carefully considered when interpreting the data in such environments.

4.7.9 Radio frequency interference

The occurrence of radio frequency interference (RFI), especially near urban areas, presents an additional challenge, as ESCAT's frequency range began to be shared with mobile telecommunication services starting in 2003. However, recent studies indicate that RFI became a significant issue in Metop ASCAT data only after the end of the ERS-2 mission in 2011. Therefore, the impact of RFI on ESCAT measurements is expected to be negligible.

5 References

[1] Vass, P., European Space Agency, Earthnet, and European Space Research Institute, *ERS-1 System* (ESA SP 1146). Noordwijk, Netherlands: ESA Publications Division, 1992.

[2] European Space Agency, *Earthnet online - the ers missions*, https://earth.esa.int/eogateway/missions/ers, Accessed on 10 June 2025, 2025.

[3] Attema, E., "The active microwave instrument on-board the ers-1 satellite," *Proceedings of the IEEE*, vol. 79, no. 6, pp. 791–799, 1991. DOI: 10.1109/5.90158.

[4] Lecomte, P., "Ers scatterometer instrument and the on-ground processing of its data," in *European Space Agency Special Publication*, ESA, 1998, pp. 241–260.

[5] Bartalis, Z., "Spaceborne scatterometers for change detection over land," Ph.D. dissertation, Technische Universität Wien, Vienna, Dec. 2009.

[6] Neyt, X., Pettiaux, P., and Acheroy, M., "Scatterometer ground processing review for gyro-less operations," in *Proceedings of SPIE - The International Society for Optical Engineering*, vol. 4880, 2002, pp. 1–10.

[7] ESA, TU Wien, TU Delft, *ESCAT Quality Assessment, Quality Control, and ASCAT Interoperability Report*, v1.1, 2025.

[8] Reimer, C., "Calibration of space-borne Scatterometers: Towards a consistent climate data record for Soil Moisture Retrieval," Vienna University of Technology, Department of Geodesy and Geoinformation, Austria, 2014. [Online]. Available: http://repositum.tuwien.ac.at/urn:nbn:at:at-ubtuw:1-70509.

[9] Harrison, C., Hahn, S., Lindorfer, R., Melzer, T., Crapolicchio, R., and Wagner, W., "Practical implementation and adaptation of rainforest-based inter-calibration for escat-ascat scatterometer data records," *ISPRS Annals of the Photogrammetry, Remote Sensing and Spatial Information Sciences*, vol. XI-3-2026, pp. 411–417, 2026. DOI: 10.5194/isprs-annals-XI-3-2026-411-2026. [Online]. Available: https://isprs-annals.copernicus.org/articles/XI-3-2026/411/2026/.

[10] Bartalis, Z., Scipal, K., and Wagner, W., "Azimuthal anisotropy of scatterometer measurements over land," *IEEE Transactions on Geoscience and Remote Sensing*, vol. 44, no. 8, pp. 2083–2092, 2006. DOI: 10.1109/TGRS.2006.872084.

[11] Dardel, C., Kergoat, L., Hiernaux, P., Mougin, E., Grippa, M., and Tucker, C. J., "Re-greening sahel: 30 years of remote sensing data and field observations (mali, niger)," *Remote Sensing of Environment*, vol. 140, pp. 350–364, 2014. DOI: https://doi.org/10.1016/j.rse.2013.09.011.

[12] Lindorfer, R., "Azimuthal anisotropy in ASCAT backscatter measurements," Technische Universität Wien, Vienna, Austria, 2024. [Online]. Available: https://doi.org/10.34726/hss.2024.120220.

[13] Hahn, S., Reimer, C., Vreugdenhil, M., Melzer, T., and Wagner, W., "Dynamic Characterization of the Incidence Angle Dependency of Backscatter Using Metop ASCAT," *IEEE Journal of Selected Topics in Applied Earth Observations and Remote Sensing*, vol. 10, no. 3, p. 12, 2016. DOI: 10.1109/JSTARS.2016.2628523.

[14] Melzer, T., "Vegetation Modelling in WARP 6.0," in *EUMETSAT Meteorological Satellite Conference*, Vienna, Austria, 2013.

[15] Hastie, T., Tibshirani, R., and Friedman, J., *The Elements of Statistical Learning : Data Mining, Inference, and Prediction*, English. New York: Springer, 2009.

[16] Frantzen, P., Steele-Dunne, S. C., Quaife, T., Vreugdenhil, M., Hahn, S., and Wagner, W., "Improved Estimation of Temporal Dynamics in the ASCAT Backscatter-Incidence Angle Relation Using Regularization," *IEEE Journal of Selected Topics in Applied Earth Observations and Remote Sensing*, vol. 18, pp. 13 457–13 471, 2025. DOI: 10.1109/JSTARS.2025.3572306. [Online]. Available: https://ieeexplore.ieee.org/document/11008820 (visited on 06/05/2025).

[17] Gelman, A., Carlin, J. B., Stern, H. S., Dunson, D. B., Vehtari, A., and Rubin, D. B., *Bayesian Data Analysis*, Third edition. CRC, 2013.

[18] Berger, J. O. and Berger, J. O., *Statistical Decision Theory and Bayesian Analysis*, Second edition. Springer New York, 1985. DOI: 10.1007/978-1-4757-4286-2.

[19] Stephen, H. and Long, D., "Microwave backscatter modeling of erg surfaces in the Sahara desert," *IEEE Transactions on Geoscience and Remote Sensing*, vol. 43, no. 2, pp. 238–247, Feb. 2005. DOI: 10.1109/TGRS.2004.840646.

[20] Wagner, W., Lindorfer, R., Melzer, T., Hahn, S., Bauer-Marschallinger, B., Morrison, K., Calvet, J.-C., Hobbs, S., Quast, R., Greimeister-Pfeil, I., and Vreugdenhil, M., "Widespread occurrence of anomalous c-band backscatter signals in arid environments caused by subsurface scattering," *Remote Sensing of Environment*, vol. 276, p. 113 025, Jul. 2022. DOI: 10.1016/j.rse.2022.113025.

[21] Wagner, W., Lindorfer, R., Hahn, S., Kim, H., Vreugdenhil, M., Gruber, A., Fischer, M., and Trnka, M., "Global scale mapping of subsurface scattering signals impacting ascat soil moisture retrievals," *IEEE Transactions on Geoscience and Remote Sensing*, vol. 62, pp. 1–20, 2024. DOI: 10.1109/TGRS.2024.3429550.

[22] Muñoz-Sabater, J., Dutra, E., Agustí-Panareda, A., Albergel, C., Arduini, G., Balsamo, G., Boussetta, S., Choulga, M., Harrigan, S., Hersbach, H., Martens, B., Miralles, D. G., Piles, M., Rodríguez-Fernández, N. J., Zsoter, E., Buontempo, C., and Thépaut, J.-N., "Era5-land: A state-of-the-art global reanalysis dataset for land applications," *Earth System Science Data*, vol. 13, no. 9, pp. 4349–4383, 2021. DOI: 10.5194/essd-13-4349-2021. [Online]. Available: https://essd.copernicus.org/articles/13/4349/2021/.

List of Tables

List of Figures

List of Acronyms

AMI Active Microwave Instrument

ASCAT Advanced Scatterometer

ATBD Algorithm Theoretical Basis Document

DoY Day of Year

ECMWF European Centre for Medium-Range Weather Forecasts

ERA5-Land ERA5-Land Surface Reanalysis from ECMWF

ERS European Remote-sensing Satellite (1 and 2)

ESA European Space Agency

ESCAT ERS-1 and ERS-2 Scatterometer

ESD Estimated Standard Deviation

FDR4LDYN Fundamental Data Record for Land Dynamics

KS Kernel Smoother

MetOp Meteorological Operational Platform

RFI Radio Frequency Interference

SAR Synthetic Aperture Radar

SCA Scatterometer on Metop-SG-B

SNR Signal-to-Noise Ratio

TU Delft Technische Universiteit Delft (Delft University of Technology)

TU Wien Technische Universität Wien (Vienna University of Technology)

VV Vertical Transmit and Vertical Receive Polarisation